PHYSICAL REVIEW B **89**, 235115 (2014)

Visualizing the charge density wave transition in 2*H*-$NbSe_2$ in real space

C. J. Arguello,[1,*] S. P. Chockalingam,[1,*] E. P. Rosenthal,[1] L. Zhao,[1] C. Gutiérrez,[1] J. H. Kang,[1] W. C. Chung,[1] R. M. Fernandes,[1] S. Jia,[2] A. J. Millis,[1] R. J. Cava,[2] and A. N. Pasupathy[1]

[1]*Department of Physics, Columbia University, New York, New York 10027, USA*

[2]*Department of Chemistry, Princeton University, Princeton, New Jersey 08540, USA*

(Received 1 July 2013; revised manuscript received 4 November 2013; published 11 June 2014)

We report the direct observation in real space of the charge density wave (CDW) phase transition in pristine 2*H*-$NbSe_2$ using atomic-resolution scanning tunneling microscopy. We find that static CDW order is established in nanoscale regions in the vicinity of defects at temperatures that are several times the bulk transition temperature T_{CDW}. On lowering the temperature, the correlation length of these patches increases steadily until CDW order is established in all of space, demonstrating the crucial role played by defects in the physics of the transition region. The nanoscale CDW order has an energy- and temperature-independent wavelength. Spectroscopic imaging measurements of the real-space phase of the CDW provide indirect evidence that an energy gap in $NbSe_2$ occurs at 0.7 eV below the Fermi energy in the CDW phase, suggesting that strong electron-lattice interactions, and not Fermi surface physics, are the dominant cause for CDW formation in $NbSe_2$.

DOI: 10.1103/PhysRevB.89.235115 PACS number(s): 71.45.Lr, 68.37.Ef, 64.70.Nd

Transition-metal dichalcogenides are quasi-two-dimensional materials, of which several show strong charge order at low temperature [1]. Our current understanding of the charge density wave (CDW) transition from the normal state is based on momentum-space probes such as neutron [2] and x-ray scattering [3], angle-resolved photoemission spectroscopy (ARPES) [4,5], optical spectroscopy [6], and Raman spectroscopy [7], which reveal a rather typical second-order transition. Several pioneering scanning tunneling microscopy (STM) spectroscopy studies have been performed deep in the charge-ordered phase near zero temperature in both pristine and doped dichalcogenides [1]. A more recent STM study linked strain with the existence of stripelike CDW at temperatures well below T_c [8]. However, none of the modern STM spectroscopic imaging techniques has been used to obtain a real-space, energy-dependent picture of either the CDW state or the CDW phase transition in the dichalcogenides. This requires precise, variable-temperature STM and scanning tunneling spectroscopy (STS) measurements through the phase transition [9]. Such studies on other complex materials like the cuprates and heavy fermions have yielded a wealth of information on the local electronic structure and have sparked many debates on the role of electronic inhomogeneity and charge order in these materials [10–12]. The dichalcogenides offer a clean test-bed to study the atomic-scale onset of a well-established CDW phase from the normal metal phase, without the complications of competing phases or strong disorder (intrinsic dilute disorder in the system will be shown to play a fundamental role on the nature of the CDW phase transition). We have performed such measurements on the prototypical CDW material $NbSe_2$, which has a bulk second-order phase transition from a normal metal phase to a nearly commensurate (3×3) charge-ordered phase at $T_{CDW} = 33.7$ K [2].

I. TOPOGRAPHIC IMAGES—CDW TEMPERATURE DEPENDENCE

A typical STM image recorded at a temperature of $T = 38$ K [Fig. 1(a)] shows three features that are common to every image that we obtain. First, we see the surface selenium atoms, which form a triangular lattice with lattice spacing of 3.44 Å. Also visible are surface and subsurface defects, such as vacancies and interstitials. The density of such defects is very low, with a residual resistivity ratio ~20, which is typical of the best crystals available. Finally, a short-range CDW is observed with a 3×3 atom periodicity in the immediate vicinity of the defects. At this temperature ($T = 1.2\ T_{CDW}$), we see that the CDW covers approximately 50% of the surface area of the sample. Below T_{CDW} [Fig. 1(b)], the CDW phase covers the entire sample area. Figures 1(c)–1(e) shows STM images taken at different locations in the vicinity of single Se vacancies at temperatures of 57, 82, and 96 K. From these images, it is apparent that the short-range CDW can be observed with STM up to temperatures of $\sim 3T_{CDW}$, with a gradual decrease in the range and coverage of the CDW with increasing temperature. At the highest temperature measured (96 K), we estimate the coverage to be close to 10%. When calculating the average coverage, images with a large field of view should be used, since the coverage at very small scales is dependent on the local defect density, which is not uniform. We did not observe any obvious dependence between the effective range of the CDW and the distance between defects at any temperature.

Our STM measurements of this short-range CDW phase in $NbSe_2$ can be compared with transport measurements [13–16] on samples from the same batch. Shown in Fig. 1(f) is the temperature dependence of the in-plane resistance of one such crystal. Consistent with previous measurements [13,15], the resistance only shows a weak signature of the CDW transition, which is better visualized in the temperature derivative of the resistance shown in Fig. 1(g). A small additional contribution to the resistance starts to become apparent below a temperature of approximately 65 K (this temperature does not have a physical significance and is determined purely by the noise of the measurement); this is apparent in Fig. 1(g) as a decrease

[*]These authors contributed equally to this paper.

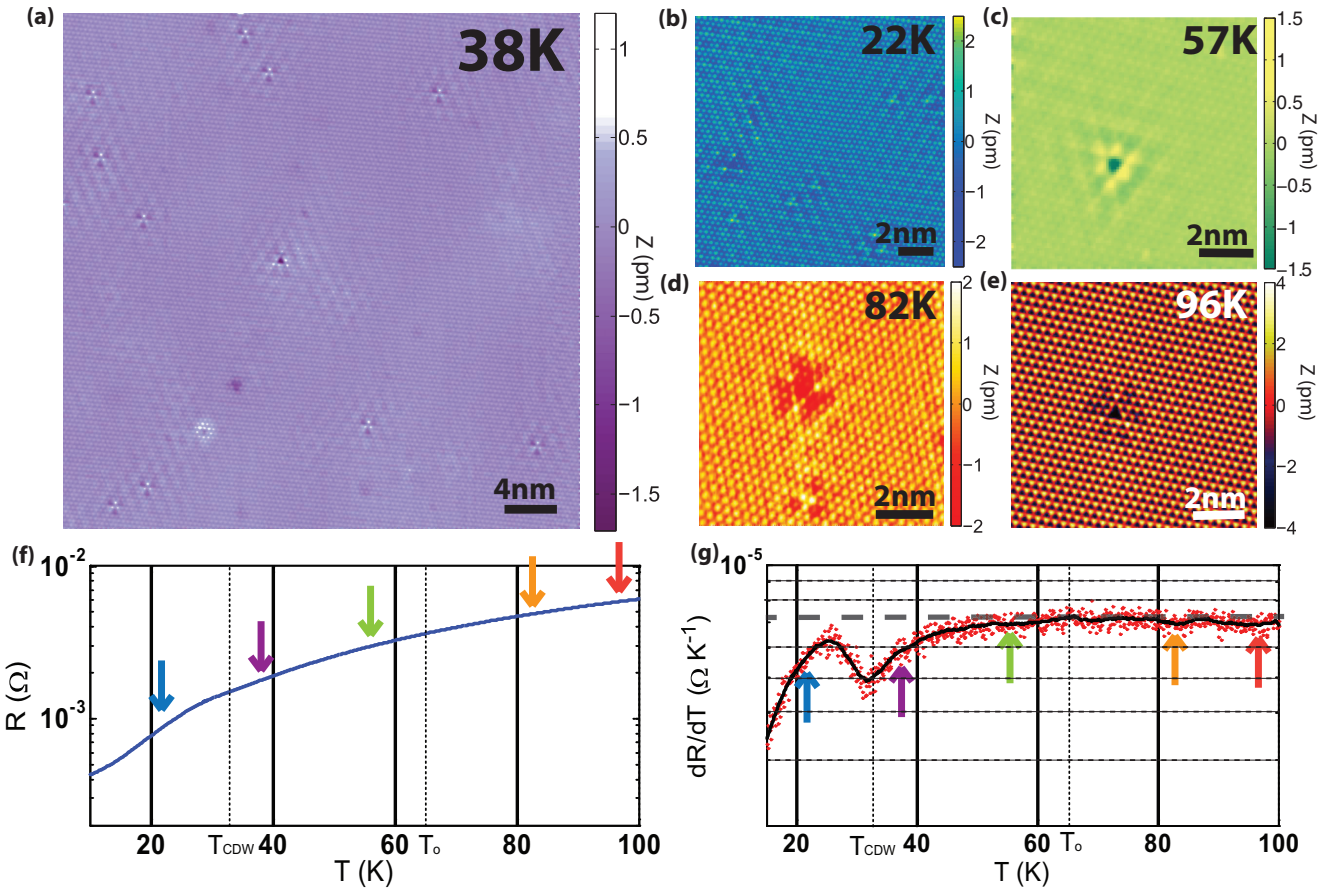

FIG. 1. (Color online) (a) STM image ($V = -100$ mV, $I = 20$ pA) of the $NbSe_2$ surface above $T_{CDW} = 33.7$ K showing surface Se, crystalline, and a short-range atomic superstructure (CDW). (b)–(e) STM images at various temperatures and different locations below and above T_{CDW}. The tunneling conditions were: at 22 K: $V = -44$ mV, $I = 150$ pA; at 57 K: $V = -200$ mV, $I = 40$ pA; at 82 K: $V = -90$ mV, $I = 50$ pA; at 96 K: $V = -230$ mV, $I = 20$ pA. (f) In-plane resistance and (g) temperature derivative of resistance of bulk samples plotted as a function of temperature. The temperatures at which the STM images are obtained are shown with color-coded arrows. On lowering the temperature below $T_O \sim 65$ K, an additional contribution is seen in the resistivity (resulting in a decrease in dR/dT from the constant value at higher temperatures).

from the constant high T value of the derivative dR/dT [dashed line, Fig. 1(g)] when $T < T_o$. This additional contribution continues to steadily increase down to T_{CDW}, at which point the resistivity starts to drop quickly. These observations are completely consistent with our STM measurements. A short-range CDW phase would increase the resistivity by providing additional potential scattering to the normal state electrons. The strength of the short-range CDW grows with decreasing temperature, resulting in stronger scattering, which is manifested by the reduction of dR/dT shown in Fig. 1(g). At T_{CDW}, the CDW establishes long-range order, and thus the potential scattering from it is suppressed. Our STM measurements of the short-range CDW above the transition temperature thus point to the key role played by even weak disorder in determining the transport properties of complex materials.

The temperature dependence of the strength of the CDW order observed can be visualized by taking the Fourier transform (FT) of large-area STM images such as the one shown in Fig. 1(a). Numerically this is done with the Fast Fourier Transform (FFT). It is important to use images with a large field of view to make meaningful comparisons of the CDW intensity in Fourier space; a small area with few defects would show an artificially suppressed intensity of the CDW peaks, which is not representative of the material studied. Figure 2(a) shows two-dimensional (2D) FT images at 22, 38, 72, and 96 K after symmetrization along the high-symmetry directions. All of the images show hexagonal spots at the atomic peak position (red) and at the CDW ordering vector (indicated by arrows). The overall intensity of each image is normalized to equalize the atomic peak intensity at each temperature. Line cuts of the FTs along the atomic ordering vector are shown in Fig. 2(b). From this image, we see that the intensity of the CDW peak decreases with increasing temperature and becomes negligible around 100 K. The CDW wavelength is temperature independent within the resolution of the STM. This is different from previous observations of temperature-dependent CDW in $NbSe_3$ [17]. In $NbSe_2$, the CDW periodicity is temperature independent, and the CDW peaks become progressively weaker with increasing temperature.

The correlation length for the short-range CDW also decreases with increasing temperature. This correlation length

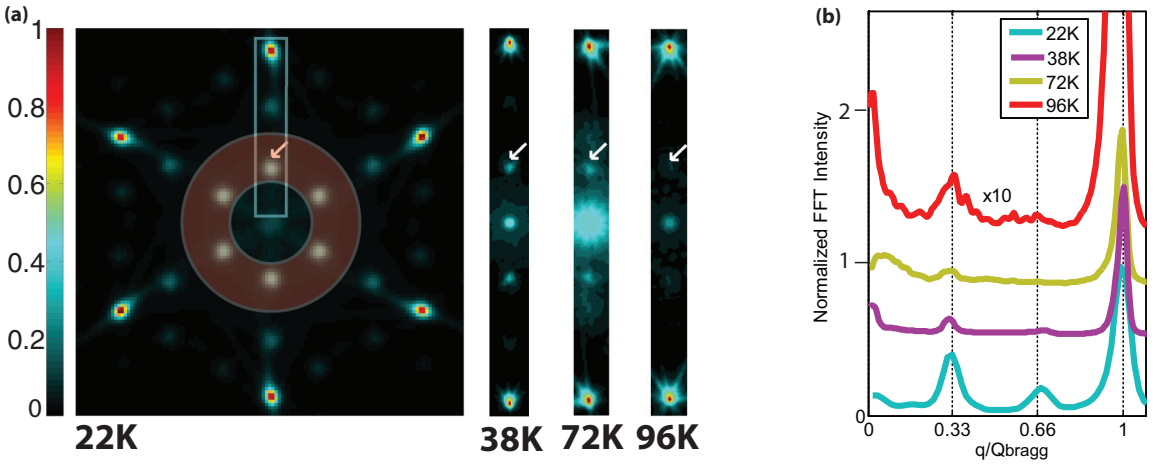

FIG. 2. (Color online) (a) (Left) FT of a 15 nm STM image obtained at 22 K. The red peaks correspond to the atomic peaks, and the CDW wave vector is marked by a white arrow. The shaded area around the CDW peaks highlights the filter used to calculate the autocorrelations shown in Fig. 3. (Right) Subsets of FT images of large-area (>30 nm) STM maps at higher temperatures. The FT images are normalized to keep the atomic peak intensity constant. The tunneling conditions for each temperature were: at 22 K: $V = 25$ mV, $I = 150$ pA; at 38 K: $V = -100$ mV, $I = 20$ pA; at 72 K: $V = 160$ mV, $I = 55$ pA; at 96 K: $V = -230$ mV, $I = 20$ pA. (b) Line cuts of FT images along an atomic wave vector at different temperatures (curves offset for clarity) showing the drop-off in CDW peak intensity with increasing temperature.

is useful to quantify the effective range of the CDW at different temperatures. In order to calculate the correlation length of the CDW at various temperatures, we Fourier filter the STM images to remove the atomic Bragg peaks using an annular band-pass filter centered at the CDW peaks as show in Fig. 2(a), with the bandwidth being several times the standard deviation of the CDW peak. We then calculate the autocorrelation $A(x) = \frac{\int f(\boldsymbol{x}')f(\boldsymbol{x}-\boldsymbol{x}')d^2x'}{\int f(\boldsymbol{x}')f(-\boldsymbol{x}')d^2x'}$ for each image. Figures 3(a)–3(d) shows autocorrelation images of the CDW at various temperatures with line cuts along the CDW modulation direction. We see that the correlation length decreases as the temperature increases. To extract the correlation length from the autocorrelation images, we first take a line cut along the x axis through the origin of the image. Each of these line cuts can be fit to a function of the form: $A(x) = A_o e^{(-x/\zeta)}\cos(k_{CDW}x) + B_o$. Here, B_o is the average of the random noise in the autocorrelation image ($B_o \ll 1$), and $A_o = 1 - B_o$. The resulting fit is shown in Fig. 3(e). Below T_c, the finite correlation length is a consequence of the finite size of the image, as well as remaining inhomogeneities of the crystal and the CDW state itself.

II. STS MEASUREMENTS

A natural question that arises is whether the short-range patterns observed in the STM images are the precursors of a true broken symmetry or have a more mundane explanation. For example, some short-range patterns that are observed in the vicinity of point defects in a metal arise from purely electronic standing waves due to quasiparticle interference (QPI) [18,19]. These patterns, called sometimes Friedel oscillations, have been reported in topographic measurements of $NbSe_3$ [20].

To address the possibility that the observed patterns arise from QPI, we obtained STS maps, in which intensity is proportional to the local density of states (LDOS), over a wide range of electron energies at temperatures above T_{CDW}. A subset of one such data set is shown in Figs. 4(a)–4(d), obtained at $T = 57$ K. It is evident from the data that the periodic patterns around each defect are observed up to the highest energies measured (±1.4 eV), though the intensity and phase of the patterns are energy dependent. A 2D-FT of one of these images is shown in Fig. 4(e).

This image displays sharp peaks at the atomic wave vector ($\boldsymbol{Q}_{\mathbf{Bragg}} = 4\pi/\sqrt{3}a_0$) as well as at the CDW wave vector

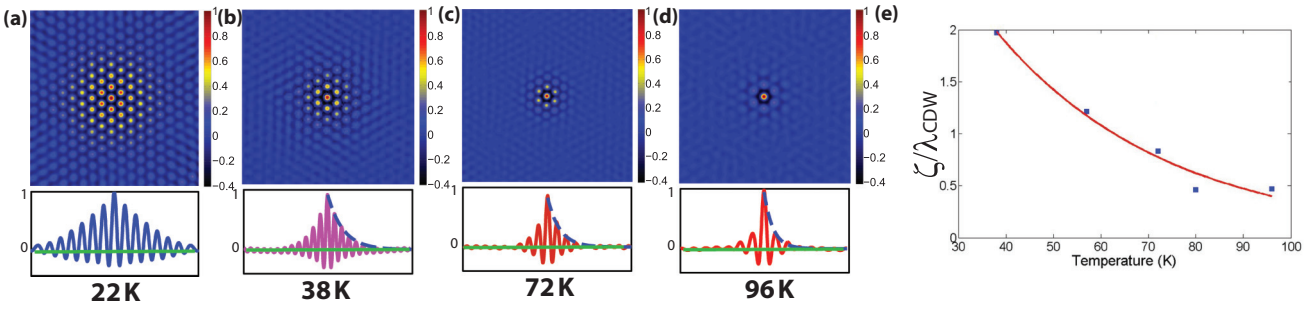

FIG. 3. (Color online) (a)–(d) Autocorrelation functions and line cuts along the atomic directions from STM images at different temperatures (the same STM images were used for the analysis of Fig. 2). The images have been Fourier-filtered to remove the atomic peak. (e) A correlation length can be extracted from the falloff of the CDW intensity as a function of distance (dashed lines) at each temperature.

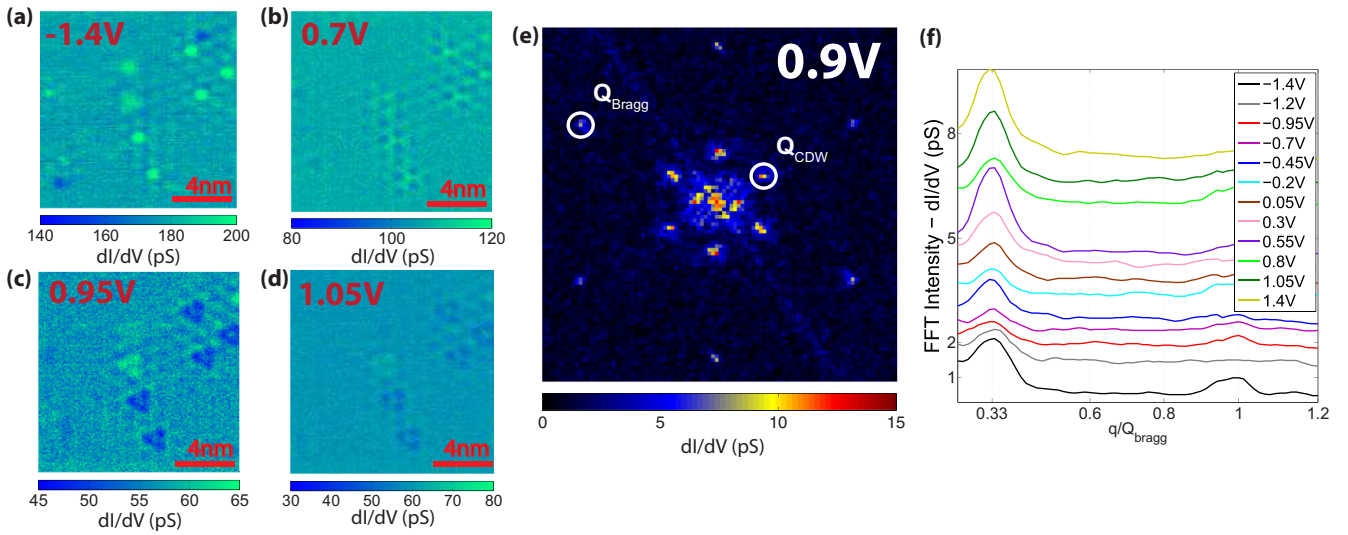

FIG. 4. (Color online) (a) dI/dV maps taken at different energies (biases) at $T = 57$ K over the same area of the $NbSe_2$ surface ($V = -1.4$ V, $I = 700$ pA). Short-range CDWs around the atomic defects are present as well as local effects of the defects themselves. (b) FT image of the dI/dV map obtained at $V = 900$ mV showing the atomic and CDW peaks but no other strong features at other wavelengths. (c) Line cut of FT images at different energies along the atomic peak direction. The CDW wave vector is seen to be independent of bias (energy).

($\boldsymbol{Q}_{\mathbf{CDW}} \sim \boldsymbol{Q}_{\mathbf{Bragg}}/3$). Similar FT images are obtained at all energies. Shown in Fig. 4(f) are line cuts at different energies of the 2D-FTs of STS maps along the atomic peak direction. We see from the line cuts that the CDW patterns seen in the STS maps have an energy-independent wavelength.

We can compare our STS observations with what we would expect in the case of QPI. In general, QPI produces patterns in Fourier space that have intensity proportional to the joint density of states (JDOS) [19]. In order to model the expected patterns in Fourier space, we performed density functional theory (DFT) calculations [21,22] of the band structure of $NbSe_2$.

The unit cell used for the DFT calculations is composed of two equivalent but shifted Se-Nb-Se subunits. The structure was allowed to relax until the forces were less than 10^{-3} Rydberg atomic units. The relaxed unit cell has a single layer Se-Se distance of 3.43 Å and a distance of 3.36 Å between top and bottom Se layers of the same subunit of the cell. The shortest Nb-Se distance is 2.60 Å. The minimum Nb-Nb distance cell is 6.26 Å. Our results are in accord with other similar calculations [21,23], and the Fermi surface [Fig. 5(a)] is consistent with recent ARPES measurements of the band structure [4,5,23,24].

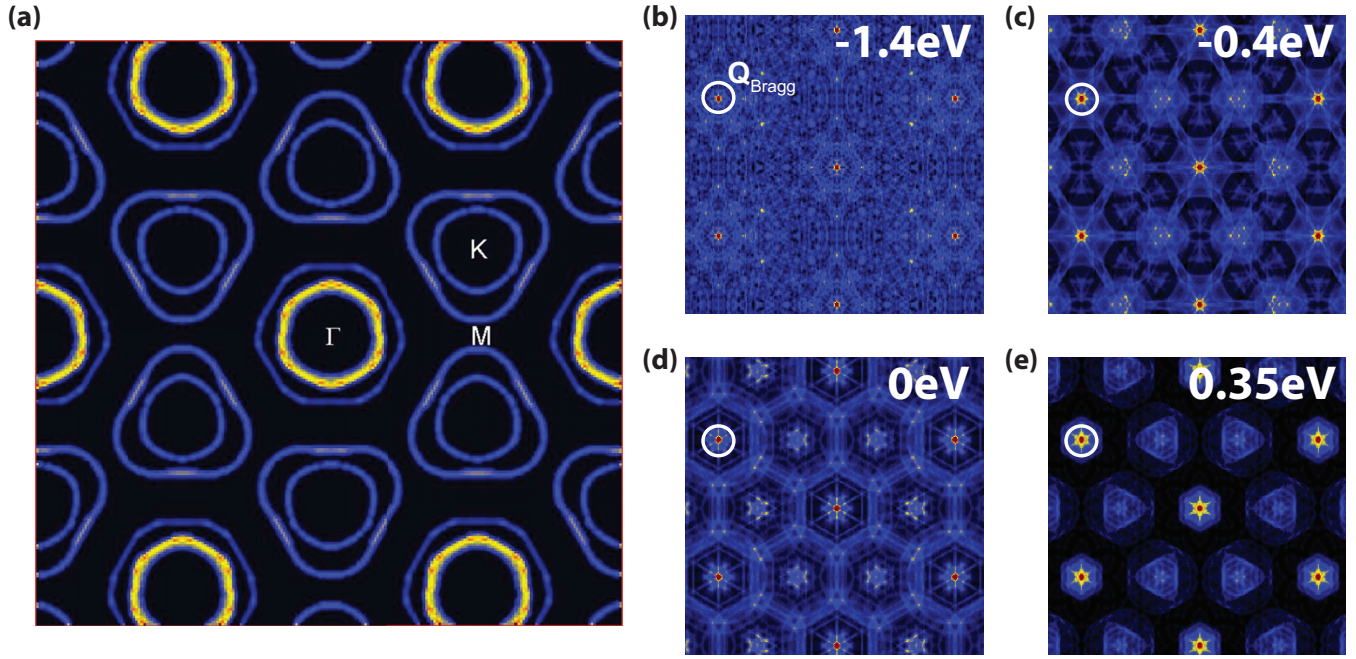

FIG. 5. (Color online) (a) Fermi surface calculated with DFT. (b)–(e) Expected scattering pattern (JDOS) from the calculated DOS of $NbSe_2$ at different energies.

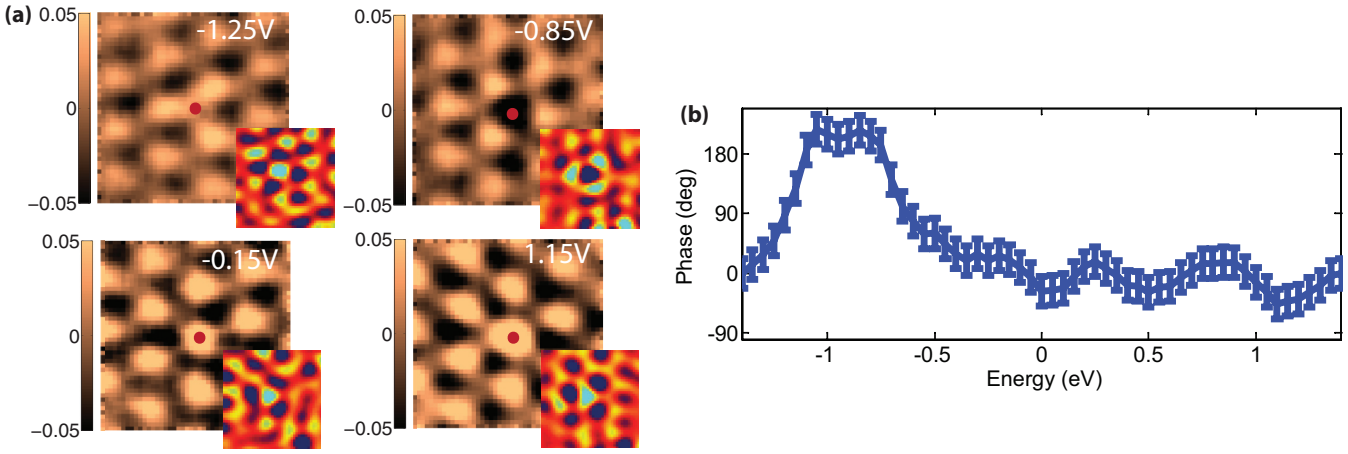

FIG. 6. (Color online) (a) Cross-correlation images between CDW band-pass filtered dI/dV maps taken at different energies (biases) at $T = 57$ K, and filtered dI/dV map taken at $V = 1.4$ V. The origin is indicated by a red dot. The CDW pattern changes from in phase (bright peak at the origin) to out of phase (origin is dark) between -0.65 and -1 V. The insets show the filtered dI/dV data in the vicinity of one defect that also illustrates this effect. (b) Extracted phase of the CDW at different energies (biases) relative to the phase at 1.4 V. Error bars given by the resolution limit of the image in pixels/degree.

Figures 5(b)–5(e) shows JDOS maps obtained at various energies from the calculations. It is evident that all of the structure seen in the JDOS maps is not seen in the STS maps; conversely, the sharp peaks seen in the STS maps at the CDW wave vectors are not seen in the JDOS maps. Essentially, the band structure of $NbSe_2$ shows significant dispersion over the volt scale, and one would expect to see the effect of this dispersion in QPI measurements (QPI generically leads to energy-dependent features). This is in direct contrast to what we observe in the experiment, indicating that the patterns seen in the experiment do not come from QPI. The fact that the observed CDW patterns show strong temperature dependence and persist out to volt-scale energies indicates that a static lattice distortion is present in the short-range CDW regime and affects electronic states at all energies.

While the CDW wavelength remains constant over a wide energy range, the intensity and phase of the modulations seen in real space vary considerably for differing energies. We can directly see this from the STS maps shown in Figs. 4(a)–4(d). In one dimension, the local phase of the CDW corresponds to whether a given point in real space corresponds to the crest (phase 0°) or trough (phase 180°) of the CDW modulation. The 2D CDW in $NbSe_2$ is therefore described by two local phases. Close observation of the images in Figs. 4(a)–4(d) shows that the crests and troughs of the CDW do not align in space for all energies. In order to track the energy dependence of the CDW phase, we calculate the 2D cross-correlation between STS images at different energies and a reference image (for which we have chosen the highest energy STS map at $E = +1.4$ eV). We are thus able to follow the relative CDW phase with respect to this reference image. To visualize only the phases associated with the CDW, we band-pass filter the STS images around the CDW wave vectors to remove the effect of any other electronic inhomogeneity that may exist. A subset of these cross-correlation functions is shown in Fig. 6(a) ($T = 57$ K). The cross-correlation functions at each energy can be fitted to extract the CDW phases, one of which is plotted in Fig. 6(b) (the other phase has similar behavior). The fitting was done by taking line cuts at each energy along $\boldsymbol{Q}_{\mathbf{CDW}}$ and fitting them to appropriate sinusoidal functions, from which the phase can be extracted. The error is given by the pixel resolution of the image.

The CDW remains in phase from $+1.4$ eV down to about -0.7 eV, when it undergoes a 180° phase shift, with a second weak reversal occurring beyond -1 eV. We eliminate the STM constant-current normalization as a cause for the phase shifts by taking topographic images at different bias setpoints. Between -0.6 V and $+1.0$ V, these images look nearly identical, whereas significant changes in the CDW are seen for images obtained with setpoints below -0.6 V (see Fig. 7). These differences prove that real variations occur in the LDOS at large negative energies in a manner consistent with the spectroscopic data shown in Figs. 4(a)–4(d).

III. TIGHT-BINDING MODEL

To understand the changes in the phase of the CDW observed in our STS measurements, we developed a minimal one-dimensional (1D) tight-binding model that captures the essential features of the system. In the normal state, each unit cell contains two types of atoms, which we associate with Se and Nb. The on-site energies at each atom are denoted by Δ_1 and Δ_2, respectively; the nearest-neighbor hopping parameter (i.e., between two atoms of different types) is given by t, and the next-nearest-neighbor hopping parameters (i.e., between two atoms of the same type) are denoted by t_1' and t_2'. This model is a 1D simplified version of the one presented in Ref. [25].

In the CDW state, two consecutive atoms of the same type can have different on-site energies $\Delta_i - \delta_i$ and $\Delta_i + \delta_i$, while two consecutive bonds between different atoms can have different hopping parameters $t + \tau$ and $t - \tau$ (see Fig. 8). In either case, the unit cell in the CDW state doubles its size. If $\delta \neq 0$ and $\tau = 0$, we have a site-centered CDW, whereas in the case of $\tau \neq 0$ and $\delta = 0$, we have a bond-centered CDW.

In the dI/dV measurements performed in the experiment, electrons tunnel into the Se atoms, which are the ones exposed after cleaving the crystal. The observed CDW contrast is the

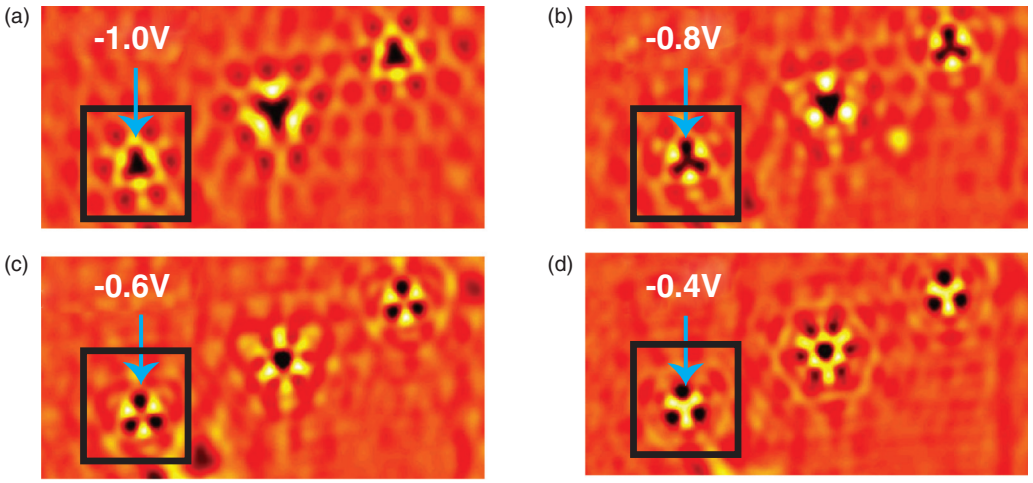

FIG. 7. (Color online) (a)–(d) Filtered topographic images showing CDW taken at different biases at $T = 57$ K. An annular band-pass filter centered on the CDW peaks [shown in Fig. 2(a)] has been used to suppress the atomic corrugation and enhance the CDW order. The CDW pattern (one of them shown enclosed in the black square) changes its phase between -1 V and -0.4 V in a consistent manner with the cross-correlation of the STS results presented in Fig. 6.

difference in the dI/dV signal between the peak and trough of the CDW in real space. In our model, this corresponds to the difference in the LDOS on adjacent Se atoms and is given by:

$$\delta\left(\frac{dI}{dV}\right) = \sum_{k,\lambda} \left(\left|u^{(\mathrm{Se})}_{k,\lambda}\right|^2 - \left|u^{(\mathrm{Se})}_{k+Q,\lambda}\right|^2\right)\delta(V - \varepsilon_{k,\lambda}) \quad (1)$$

where $u^{(\mathrm{Se})}_{k,\lambda}$ is the Se-atom component of the eigenfunction associated with the energy state $\varepsilon_{k,\lambda}$. A sign change in this quantity corresponds to a 180° change in the phase of the CDW, as seen in the STS maps. Here, k is the momentum, λ is the band index, and Q is the modulation vector of the CDW.

In the normal state, $|u^{(\mathrm{Se})}_{k,\lambda}|^2 = |u^{(\mathrm{Se})}_{k+Q,\lambda}|^2$, and the contrast is zero, as expected. To study how these eigenfunctions change in the CDW state, it is enough to focus at the Bragg points $\varepsilon_{k,\lambda} = \varepsilon_{k+Q,\lambda}$, where the CDW gap opens. For simplicity, hereafter we assume that only the variation of the red ("Se") site energy $\delta_1 \neq 0$. Then, after defining $\Delta \equiv \Delta_1 - \Delta_2$, the Hamiltonian of the system at the Bragg points is

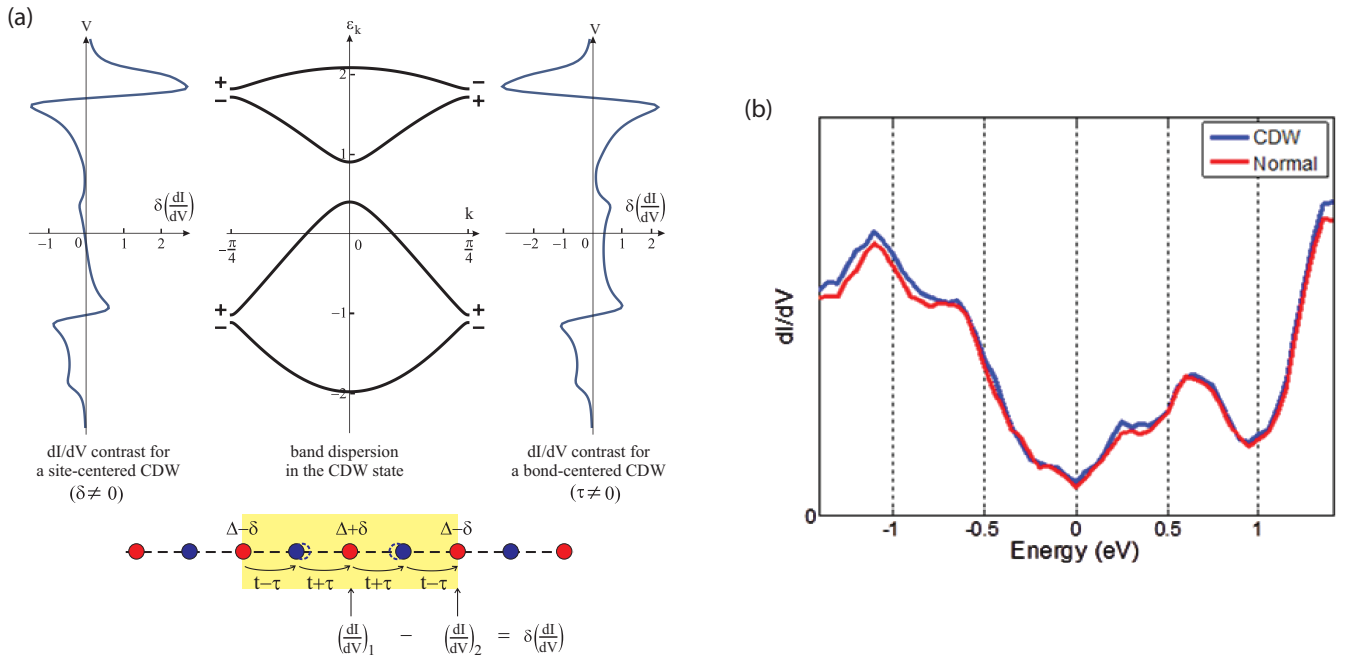

FIG. 8. (Color online) (a) Summary of the 1D tight-binding model results. The two different types of CDW lead to two different phase behaviors. A gap at $\vec{K}_{\mathrm{CDW}}$ for $E \simeq -0.7$ eV is to be expected from our experimental results. (b) Experimental average dI/dV curves (in arbitrary units) for a CDW patch (blue) and for normal state (blue), taken at $T = 57$ K. There are not obvious differences between these two spectra.

given by:

$$\mathcal{H}_{\text{Bragg}} = \Psi^{\dagger}_{k_{\text{Bragg}}} \begin{pmatrix} 2(\Delta+\delta) & 0 & -(t-\tau) & t-\tau \\ 0 & 2(\Delta-\delta) & -(t+\tau) & -(t+\tau) \\ -(t-\tau) & -(t+\tau) & 0 & 0 \\ t-\tau & -(t+\tau) & 0 & 0 \end{pmatrix} \Psi_{k_{\text{Bragg}}} \tag{2}$$

where we defined the creation operators:

$$\Psi^{\dagger}_{k} = (c^{\dagger}_{k,\text{Se}},\, c^{\dagger}_{k+Q,\text{Se}},\, c^{\dagger}_{k,\text{Nb}},\, c^{\dagger}_{k+Q,\text{Nb}}) \tag{3}$$

We study separately the two possible CDW scenarios, i.e., site-CSW ($\delta \neq 0$ and $\tau = 0$) and bond-CDW ($\delta = 0$ and $\tau \neq 0$). To calculate the eigenfunctions, we use standard degenerate first-order perturbation theory with the unperturbed Hamiltonian $H_0 = H_{\text{Bragg}}(\delta = \tau = 0)$, and the perturbations $H_1 = H_{\text{Bragg}}(\delta \ll \Delta, \tau = 0) - H_0$ for site-CDW and $H_1 = H_{\text{Bragg}}(\delta = 0, \tau \ll t) - H_0$ for bond-CDW.

The diagonalization of H_0 yields two sets of doubly degenerate energy eigenstates, corresponding to the upper and lower bands:

$$E_U \equiv \Delta + \sqrt{2t^2+\Delta^2} > 0; \quad E_L \equiv \Delta - \sqrt{2t^2+\Delta^2} < 0 \tag{4}$$

each with eigenvectors:

$$u_{i,1} = (E_i,\, 0,\, -1,\, 1); \quad u_{i,2} = (0,\, E_i,\, 1,\, 1), \quad i = L, U \tag{5}$$

This degeneracy is lifted by either site or bond perturbations, which are both diagonal on the basis set of Eq. (5). However, each case yields different results for the sign-change of the contrast across the two CDW gaps.

For concreteness, we consider the case $\delta > 0$ and $\tau > 0$. For site-CDW, the eigenvalue associated with the eigenstate $u_{i,1}$ is always greater than the one associated with $u_{i,2}$:

$$E_{i,(1,2)} = E_i \pm \delta \frac{E_i^2}{|E_i|\sqrt{2t^2+\Delta^2}} \tag{6}$$

since the first-order correction is proportional to the square of the unperturbed energy values. This implies that, for both upper and lower bands, the highest energy state has $|u^{(\text{Se})}_{k,\lambda}|^2 > |u^{(\text{Se})}_{k+Q,\lambda}|^2$, whereas the lowest energy state has $|u^{(\text{Se})}_{k,\lambda}|^2 < |u^{(\text{Se})}_{k+Q,\lambda}|^2$. Therefore, the contrast $\delta(\frac{dI}{dV})$ changes its sign from negative to positive when the CDW gap is crossed from lower to higher energies. As a result, in the site-centered case, the contrast has to change signs an odd number of times between the two energies corresponding to the two gaps.

On the other hand, for bond-CDW, the first-order correction to each eigenvalue is linearly proportional to its unperturbed values:

$$E_{i,(1,2)} = E_i \mp \tau \frac{2E_i t}{|E_i|\sqrt{2t^2+\Delta^2}} \tag{7}$$

Thus, for the lower band, since $E_L < 0$, the eigenvalue associated with $u_{L,1}$ is greater than the eigenvalue associated with $u_{L,2}$, implying that the contrast changes its sign from negative to positive when the gap is crossed from lower to higher energies. The opposite is true for the upper band, and the contrast changes its sign from positive to negative when coming from lower energies. Consequently, in the bond-centered case, the contrast must either not change its sign or change it an even number of times between the energies where the two CDW gaps open. The results of the calculation are summarized in Fig. 8.

In summary, our calculations show that the phase changes take place at the energies corresponding to the largest CDW-induced mixing between states, i.e., at the energies where the gaps open, and the magnitude of the contrast is proportional to the size of the CDW gap. An energy-dependent phase was also presented in [25]. However, experimentally we did not observe the intricate patterns described in their work, and our observations can be described as a simple contrast reversal of the CDW supported by our simplified model.

Our STS measurements therefore suggest that strong spectroscopic changes happen at the CDW wave vector at an energy of -0.7 eV, with only weak changes at the Fermi energy. There is no evidence of a CDW gap at -0.7 eV from our point spectroscopy measurements [Fig. 8(b)]. This is not unexpected because the CDW gap may have strong momentum dependence, and point spectroscopy averages over momentum space.

In order to understand why the energy region around -0.7 eV is special in $NbSe_2$, we look closely at the electronic structure of the material. Shown in Fig. 9(a) are the DFT bands projected on the Se states (green) and Nb states (red) at various energies along the CDW wave-vector direction. These figures show that there is no significant nesting at energies near or above the Fermi energy. However, at energies around -0.6 eV, we see that the electronic structure is strongly nested with the CDW wave vector [see Fig. 9(b), shaded region]. Thus, at this energy range, we expect significant hybridization to occur in the CDW state along with the consequent opening of an energy gap. This key observation is in complete agreement with our experimental measurement of a change in the phase of the CDW in this energy range.

IV. SUMMARY

In the classic Peierls transition, the driving force for CDW formation is the electronic kinetic energy gain that occurs when strong Fermi surface nesting is present. In this mechanism, the important changes to electronic structure occur close to the Fermi energy (within a few kT_{CDW}), and higher energy states are inconsequential. Our experimental measurements combined with our model suggest that the primary changes to the electronic structure when we enter the CDW phase are at much higher energies. This indicates that the Peierls mechanism is not the driving force for the CDW observed in $NbSe_2$. Rather, a strong coupling between the electrons and the lattice is essential for the formation of the CDW [26],

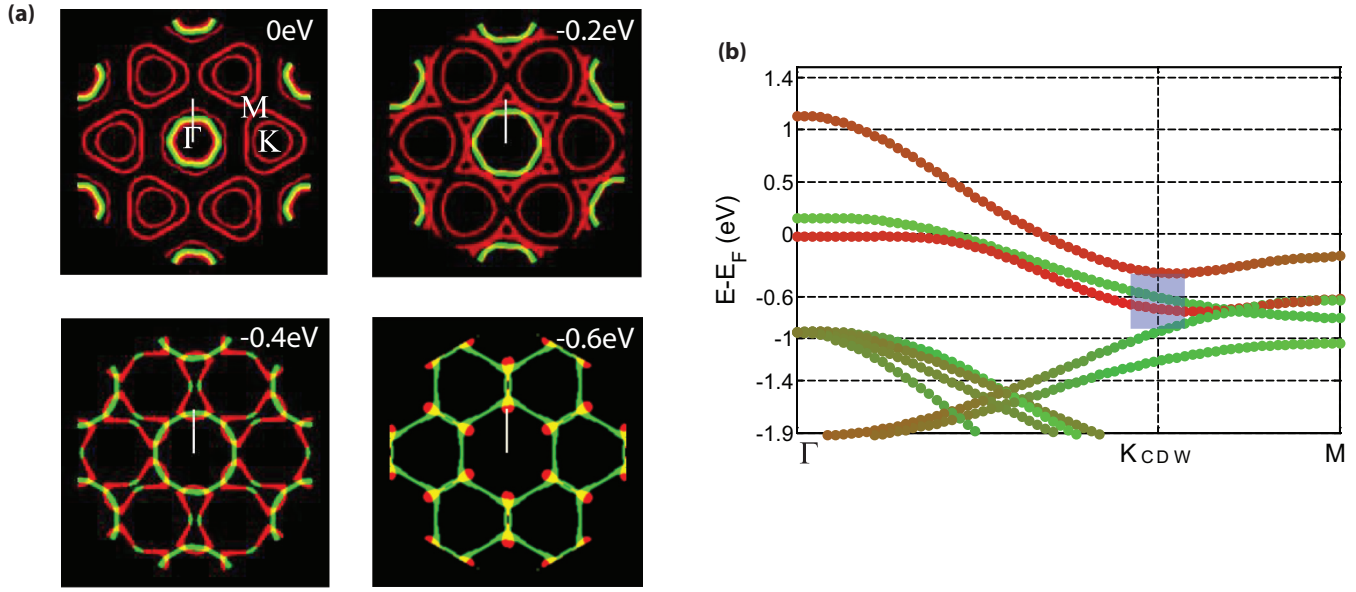

FIG. 9. (Color online) (a) Calculated DOS (Nb-like orbitals in red, Se-like orbitals in green) at different energies. At energies close to −0.6 eV, significant intensity is present at the CDW wave vectors (large nesting), whereas this is not true at other energies shown. (b) Calculated band structure projection onto Nb (red) and Se (green) orbitals along the CDW direction showing that conditions for a gap opening at the CDW Bragg point are in the vicinity of −0.6 eV (shaded blue area).

in which the presence of defects plays an important role for temperatures above the bulk transition temperature, as has been reported in other 2D and quasi-2D systems [27,28,29]. These defects could play a role in stabilizing possible 2D dynamical fluctuations present at temperatures greater than the bulk transition temperature [30], although to the best of our knowledge, no tail in the order parameter has been observed above T_c with scattering probes in $NbSe_2$. Even though our resistivity measurements are consistent with the STM results, x-ray measurements are also necessary to confirm the existence of short-range order at temperatures above T_c in the bulk. Our STS measurements for $NbSe_2$ also bear striking resemblance to the static patterns observed in the pseudogap phase of the cuprates [10–12,31], which have been associated with the CDW. However, a direct comparison between the two materials reveals two important differences. First, the cuprates show strong spatial patterns at energies within the pseudogap, with a diminishing strength at higher energies [11,12]. Second, no real-space phase change occurs in the cuprate spatial patterns while crossing the cuprate pseudogap. These two facts together imply that the spatial pattern seen by STM in the cuprate pseudogap state is not a simple CDW gap of the type seen in $NbSe_2$.

Most importantly, we demonstrate that (as has been speculated theoretically [32]) the homogeneous normal state of this system is extremely fragile around impurities, leading to large patches of static order even very far from the phase boundary, despite the fact that impurities are very dilute in this system. This in turn fundamentally affects all macroscopic observables, including transport coefficients [14,15], scattering measurements [3], and spectroscopic properties [5]. Anomalous experimental measurements in these materials should be reinterpreted in light of our findings, and new theoretical tools should be developed for these materials in the regime of localized, static order.

ACKNOWLEDGMENTS

We thank D. Efetov for experimental help and V. Oganesyan for discussions. Salary support has been provided by the U.S. National Science Foundation under the Materials Interdisciplinary Research Team (S.P.C., Grant No. DMR-1122594), by the Partnership for International Research and Education (R.M.F., A.J.M., and A.N.P., Grant No. OISE-0968226) and CAREER (A.N.P., Grant No. DMR-1056527) programs, by DMR-1006282 (A.J.M.), and by the Air Force Office of Scientific Research under Grant FA9550-11-1-0010 (A.N.P.). The crystal growth at Princeton was supported by the Department of Energy Basic Energy Sciences Grant DE-FG02-98ER45706 (R.J.C.).

[1] R. V. Coleman, B. Giambattista, P. K. Hansma, A. Johnson, W. W. McNairy, and C. G. Slough, Adv. Phys. **37**, 559 (1988).
[2] D. E. Moncton, J. D. Axe, and F. J. DiSalvo, Phys. Rev. Lett. **34**, 734 (1975).
[3] Y. Feng, J. Wang, R. Jaramillo, J. van Wezel, S. Haravifard, G. Srajer, Y. Liu, Z.-A. Xu, P. B. Littlewood, and T. F. Rosenbaum, Proc. Natl. Acad. Sci. U.S.A. **109**, 7224 (2012).
[4] T. Kiss, T. Yokoya, A. Chainani, S. Shin, T. Hanaguri, M. Nohara, and H. Takagi, Nat. Phys. **3**, 720 (2007).
[5] S. V. Borisenko, A. A. Kordyuk, V. B. Zabolotnyy, D. S. Inosov, D. Evtushinsky, B. Büchner, A. N. Yaresko, A. Varykhalov,

R. Follath, W. Eberhardt, L. Patthey, and H. Berger, Phys. Rev. Lett. **102**, 166402 (2009).
[6] S. V. Dordevic, D. N. Basov, R. C. Dynes, and E. Bucher, Phys. Rev. B **64**, 161103 (2001).
[7] F. Weber, S. Rosenkranz, J. P. Castellan, R. Osborn, R. Hott, R. Heid, K. P. Bohnen, T. Egami, A. H. Said, and D. Reznik, Phys. Rev. Lett. **107**, 107403 (2011).
[8] A. Soumyanarayanan, M. M. Yee, Y. He, J. van Wezel, D. J. Rahn, K. Rossnagel, E. W. Hudson, M. R. Norman, and J. E. Hoffman, PNAS **110**, 1623 (2013).
[9] K. K. Gomes, A. N. Pasupathy, A. Pushp, S. Ono, Y. Ando, and A. Yazdani, Nature **447**, 569 (2007).
[10] Y. Kohsaka, C. Taylor, K. Fujita, A. Schmidt, C. Lupien, T. Hanaguri, M. Azuma, M. Takano, H. Eisaki, H. Takagi, S. Uchida, and J. C. Davis, Science **315**, 1380 (2007).
[11] M. Vershinin, S. Misra, S. Ono, Y. Abe, Y. Ando, and A. Yazdani, Science **303**, 1995 (2004).
[12] W. D. Wise, M. C. Boyer, K. Chatterjee, T. Kondo, T. Takeuchi, H. Ikuta, Y. Wang, and E. W. Hudson, Nat. Phys. **4**, 696 (2008).
[13] H. N. S. Lee, M. Garcia, H. McKinzie, and A. Wold, J. Solid State Chem. **1**, 190 (1970).
[14] R. Bel, K. Behnia, and H. Berger, Phys. Rev. Lett. **91**, 066602 (2003).
[15] J. Edwards and R. F. Frindt, J. Phys. Chem. Solids **32**, 2217 (1971).
[16] J. M. E. Harper, T. H. Geballe, and F. J. Disalvo, Phys. Lett. A **54**, 27 (1975).
[17] C. Brun, Z. Z. Wang, P. Monceau, and S. Brazovskii, Phys. Rev. Lett. **104**, 256403 (2010).
[18] M. F. Crommie, C. P. Lutz, and D. M. Eigler, Nature **363**, 524 (1993).
[19] K. McElroy, R. W. Simmonds, J. E. Hoffman, D.-H. Lee, J. Orenstein, H. Eisaki, S. Uchida, and J. C. Davis, Nature **422**, 592 (2003).
[20] S. Brazovskii, C. Brun, Z.-Z. Wang, and P. Monceau, Phys. Rev. Lett. **108**, 096801 (2012).
[21] M. D. Johannes and I. I. Mazin, Phys. Rev. B **77**, 165135 (2008).
[22] P. Giannozzi, S. Baroni, N. Bonini, M. Calandra, R. Car, C. Cavazzoni, D. Ceresoli, G. L. Chiarotti, M. Cococcioni, I. Dabo *et al.*, J. Phys.: Condens. Matter **21**, 395502 (2009).
[23] K. Rossnagel, O. Seifarth, L. Kipp, M. Skibowski, D. Voss, P. Krüger, A. Mazur, and J. Pollmann, Phys. Rev. B **64**, 235119 (2001).
[24] T. Valla, A. V. Fedorov, P. D. Johnson, P. A. Glans, C. McGuinness, K. E. Smith, E. Y. Andrei, and H. Berger, Phys. Rev. Lett. **92**, 086401 (2004).
[25] W. Sacks, D. Roditchev, and J. Klein, Phys. Rev. B **57**, 13118 (1998).
[26] C. M. Varma and A. L. Simons, Phys. Rev. Lett. **51**, 138 (1983).
[27] A. V. Melechko, J. Braun, H. H. Weitering, and E. W. Plummer, Phys. Rev. Lett. **83**, 999 (1999).
[28] I. Brihuega, O. Custance, R. Perez, and J. M. Gomez-Rodriguez, Phys. Rev. Lett. **94**, 046101 (2005).
[29] J. Ishioka, T. Fujii, K. Katono, K. Ichimura, T. Kurosawa, M. Oda, and S. Tanda, Phys. Rev. B **84**, 245125 (2011).
[30] S. Girault, A. H. Moudden, and J. P. Pouget, Phys. Rev. B **39**, 4430 (1989).
[31] T. Hanaguri, C. Lupien, Y. Kohsaka, D.-H. Lee, M. Azuma, M. Takano, H. Takagi, and J. C. Davis, Nature **430**, 1001 (2004).
[32] A. J. Millis, Solid State Commun. **126**, 3 (2003).